

¹ Centro di Eccellenza CETEMPS, Università dell’Aquila, L’Aquila, Italy

² Dipartimento di Fisica, Università dell’Aquila, L’Aquila, Italy

³ Dipartimento di Ingegneria Elettronica, Università “La Sapienza” di Roma, Rome, Italy

⁴ Centro Funzionale Protezione Civile, Regione Abruzzo, L’Aquila, Italy

Flood forecast in complex orography coupling distributed hydro-meteorological models and in-situ and remote sensing data

**M. Verdecchia^{1,2}, E. Coppola¹, C. Faccani¹, R. Ferretti^{1,2}, A. Memmo¹,
M. Montopoli¹, G. Rivolta¹, T. Paolucci⁴, E. Picciotti⁴, A. Santacasa⁴, B. Tomassetti¹,
G. Visconti^{1,2}, F. S. Marzano^{1,3}**

With 12 Figures

Received 7 April 2006; Accepted 15 September 2007

Published online 24 October 2008 © Springer-Verlag 2008

Summary

A flood forecast chain, developed at the Centre of Excellence for Remote Sensing and Hydro-Meteorology (CETEMPS) and based on coupled mesoscale atmospheric and a newly developed distributed hydrological model with in-situ and remote sensing data integration, is illustrated. The focus is on small-catchment flood forecast in complex topography in Central Italy, but the developed modelling and processing integrated tools may be easily applied to any geographical and orographic scenario. Emphasis is put on the integration of numerical models and retrieval algorithms with aim to provide an overview of an objective system for hydro-meteorological alert-map emission. As an example, the forecast hydro-meteorological chain is applied to a case study of an extreme event on 23–25 January 2003 and results are discussed.

1. Introduction

Forecast, detection and warning of severe weather and related hydro-geological risks is becoming one of the major issues for civil protection

and land use management (Siccardi et al. 2005). In the Mediterranean area floods, even in the form of flash floods, represent a recurrent problem, especially during the fall season. The damages associated to these events are historically very significant both in terms of human and social costs and losses of unique architectural properties (Roth et al. 2004). The hydrological risk is usually further enhanced, as in the case of the Italian peninsula, by the complex topography which is characterized by small catchments along most coastlines and by the Alpine and Apennine ranges (Buzzi and Tibaldi 1977; Buzzi et al. 1998; Bougeault et al. 2001; Rotunno and Ferretti 2001). Going from north to south, the Apennine divides central and southern Italy in two main geographical areas along the Tyrrhenian, the Adriatic and Ionic seas.

This scenario, characterized by apparent geographical constraints as well as localized and extreme rainfall events, invites to exploit remote sensing systems both from satellites, such as geostationary and low-orbit radiometers (e.g., Vicente et al. 1998; Bellerby et al. 2000; Turk

Correspondence: Frank S. Marzano, Centro di Eccellenza CETEMPS, Università dell’Aquila, L’Aquila, Italy; Dipartimento di Ingegneria Elettronica, Università “La Sapienza” di Roma, Rome, Italy (E-mail: marzano@ing.univaq.it)

et al. 2000; Bennartz and Petty 2001; Marzano et al. 2002a; Ebert et al. 2007) and from ground, such as weather radar networks and microwave radiometers (e.g., Bringi and Chandrasekar 2001; Marzano et al. 2002b, 2004b; Fornasiero et al. 2005). These two data sources need to be integrated as weather radars can give highly resolved rainfall products, but their spatial coverage is not uniform and complicated by the orographic blockages, whilst satellite rain retrievals can be globally provided but at a quite coarse spatial resolution (Marzano et al. 2004a, b). Moreover, the coupling of rain remote sensing data with regional rain gauge networks is also essential for ensuring a calibration of remotely sensed rainfall fields in terms of ground effects (Grimes et al. 2003; Coppola et al. 2006). An overwhelming issue is the spatial integration of these rainfall data sources having different space-time resolution and variable accuracies.

A forecast chain needs to be based on space-time hydro-meteorological numerical models to project the current status of atmosphere and river basins into a scientifically-based prediction. Forecast hydro-meteorological models in complex topography should have some peculiar features: (i) to be usable at high spatial resolution (order of kilometre or even less) in order to resolve localized convective phenomena (Ferretti et al. 2003a, b); (ii) to be coupled in terms of assimilating geophysical field observations provided by remote and local sensors and in terms of consistency of surface-atmosphere boundary conditions (Faccani et al. 2005; Tomassetti et al. 2005 etc.). This implies that general circulation atmospheric model outputs cannot be used and we need to resort to limited area models (LAMs), possibly nested towards high spatial resolution with microphysical prognostic schemes (Colle et al. 2005; Garvert et al. 2005; Memmo et al. 2006; Serafin and Ferretti 2007). On the other hand, a physically parameterized distributed hydrological model represents an adequate tool to ingest data from both measuring sensors and atmospheric models. Last but not least, this coupled observing and forecasting system should be computationally efficient in order to be run operationally at a hydro-meteorological centre to provide realtime bulletins to civil protection decision makers. In this work, we summarize the

interdisciplinary work carried out at the Centre of Excellence for Remote Sensing and Hydro-Meteorology (CETEMPS) having in mind the above mentioned issues and the objective to approach the problem in a synergic way. A coupled mesoscale atmospheric model and distributed hydrological model with in-situ and remote sensing data integration for small-catchment flood forecast in complex topography is illustrated in detail. The various components of the hydro-meteorological chain are described and applied to a case study of an extreme event on 23–25 January 2003. Emphasis is put on the integration of numerical models and retrieval algorithms with the aim to provide an overview of an objective system for hydro-meteorological alerts. This approach, whose implications are well described in Siccardi et al. (2005), are beyond the scopes of this work. In a way, we believe that before setting a LAM-based ensemble prediction system (LEPS), the single component of the deterministic forecast chain should be tested and validated as much as possible to be eventually statistically merged.

The paper is organized as follows. Section 2 shows an overview of the CETEMPS flood forecast chain, whereas Sect. 3 is devoted to the illustration of the case study of 23–25 January 2003, taken as a leitmotiv to describe the entire chain. Section 4 gives the illustration of the remote sensing data analysis underlining all the available components. Section 5 is focused on the atmospheric modelling and forecasting models by stressing their advanced features. Section 6 deals with hydrological distributed model description, whilst Sect. 7 discussed the data integration and the application to alert mapping. Conclusions are given in Sect. 8.

2. Overview of the CETEMPS flood forecast chain

The CETEMPS flood forecast chain is illustrated in Fig. 1 by means of a block diagram and flow chart. The philosophy behind follows and tries to answer to the main issues rose in the introduction. Remote sensing data, derived from satellites, are integrated and processed to provide rainfall fields or used for short-term rain nowcasting. If available, rain products derived from weather radar are also used. These

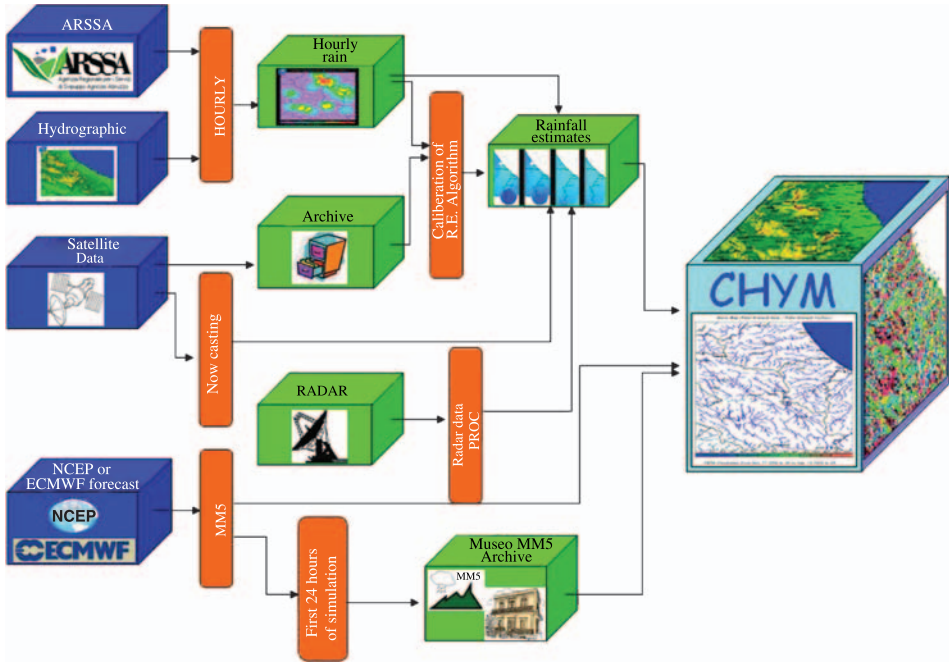


Fig. 1. Block diagram of the CETEMPS flood forecast chain. Raingauge data are those identified by ARSSA (Regional Agency for Agriculture Services) and Hydrographic institute, while meteorological analyses can come either from the European Centre for Medium-range Weather Forecast (ECMWF) or form the National Centre for Environmental Protection (NCEP). The forecast meteorological model is the Mesoscale Model 5 (MM5), while the hydrological forecast model is the CETEMPS hydrological model (CHyM)

rainfall fields are further spatially integrated with rain gauge network data and with model-forecasted precipitation fields. The latter are derived from a mesoscale high-resolution atmospheric model at primitive equations, initialized on a domain covering Italy at 27-km grid resolution downscaled to 3 km through 3 successive nested grids. Finally, the rain fields simulated in the innermost domain are used as input for a distributed hydrological model implemented on the water flow network of the region of interest.

Alert mapping is accomplished by taking into consideration the water drained over a given region with respect to given drained area by this region. Objective criteria translate these maps into a hydro-meteorological intuitive information in support of civil protection decisions, as discussed in Sect. 7.

3. Case study of an extreme flood event

In the following sub-sections we will first describe the case study and then make a list of available data.

3.1 Meteorological description

During January 23, 2003 a cyclogenesis on the Gulf of Genoa was associated to a secondary minimum located on the medium Adriatic Sea (see Fig. 2). At upper level an intrusion of cold air from northeast associated to a trough extending from Scandinavia to South Mediterranean region was present. The low-level advection of warm and humid air from South-East on the Adriatic region justifies the observed convective precipitation from the lightning map (Fig. 3). The following 24 hours were characterized by the deepening of the surface pressure minimum located in the central south Tyrrhenian sea.

At upper level a cut off low was developing associated to a cold air intrusion (Fig. 2a). Still electrical activity was detected during the night in the medium and low Adriatic sea as shown by the lightning maps (Fig. 3a), suggesting that convective activity was still under course over Abruzzo and Molise regions. During January 25 the upper level cut off low was completely in phase with the surface low (Fig. 2b) and located over Sicily. Low-level advection of warm

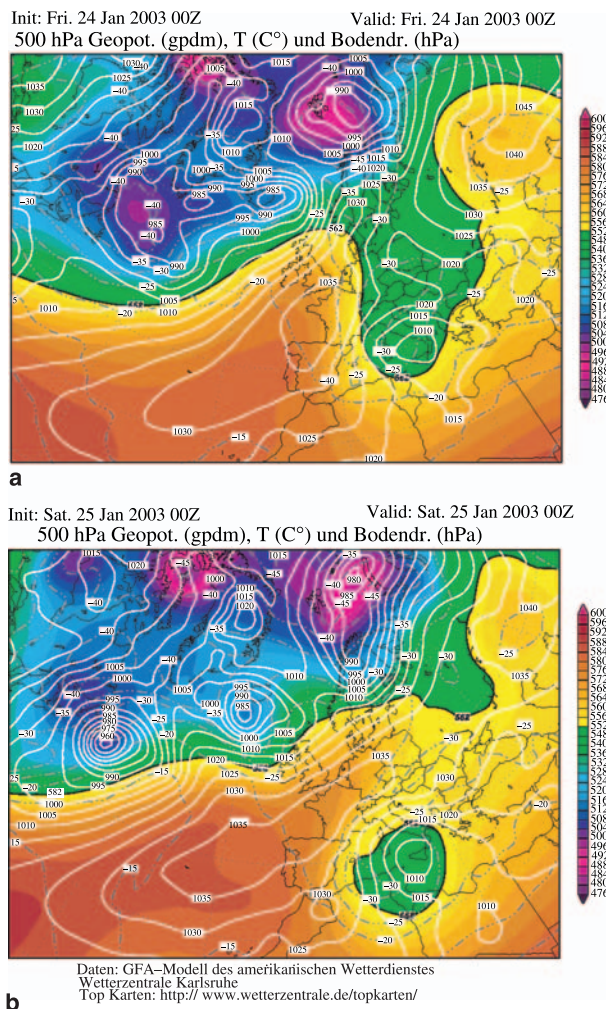


Fig. 2. Geopotential height at 500 hPa (color) and mean sea level pressure (contour lines) for: (a) 24 January at 00 UTC; (b) 25 January at 00 UTC

and humid air on the southern Italy produced convection as the intense electrical activity recorded on the South Mediterranean Sea suggests (Fig. 3b). Over Abruzzo weather conditions were improving at that time. During the following 24 hours the cyclonic system moved toward East.

The data recorded from the rain gauge clearly shows rainfall insisting over Abruzzo during the whole period. It has to be noticed that the maximum of rainfall intensity were not exceeding 20 mm/h (shown later on in Sect. 5.2) at most of the stations, except for Lanciano in Southern Abruzzo region where values exceeding 45 mm/h were recorded both at the beginning and at the end of the event. The spatial and temporal distribution of these rainfall values

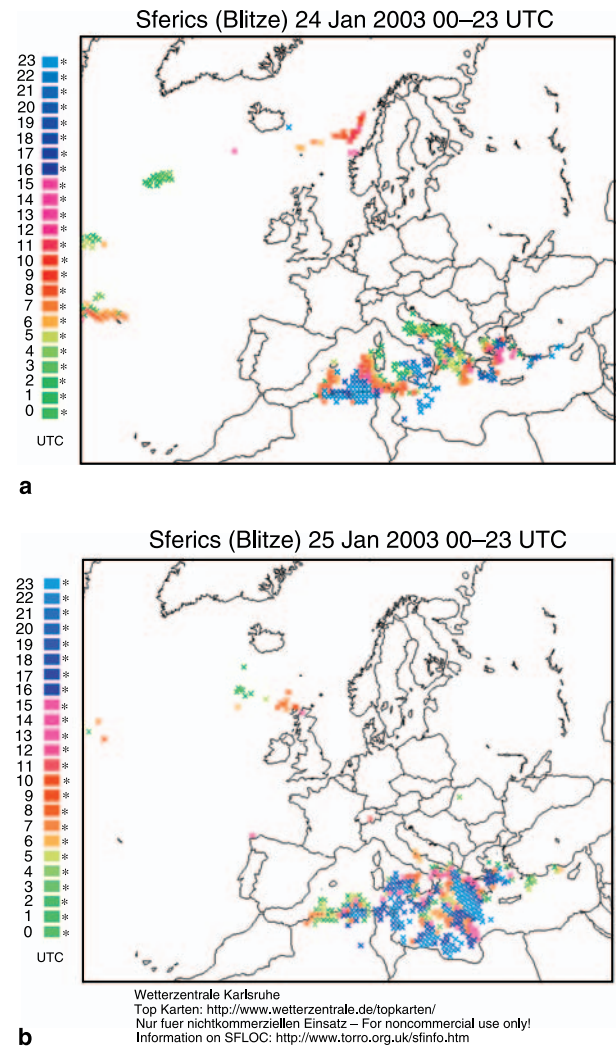


Fig. 3. Time evolution and intensity of the lightning over Europe for: (a) 24 January; (b) 25 January, measured by Sferics network (courtesy of DWD)

clearly suggests the formation of so called orographic precipitation with embedded localized convective rainfall.

The strength of this event can be measured, for instance, in terms of the damages caused to infrastructures and buildings. The next figures quantify these two aspects giving an example of the damages occurred in Abruzzo. Heavy damages were caused by this event: 110 families were evacuated due to the damages to buildings, flooding and landslide occurred at several locations as local newspapers reported. A detailed distribution of observed landslide event is shown in Fig. 4b. The regional authorities estimated damages for a total amount of several millions

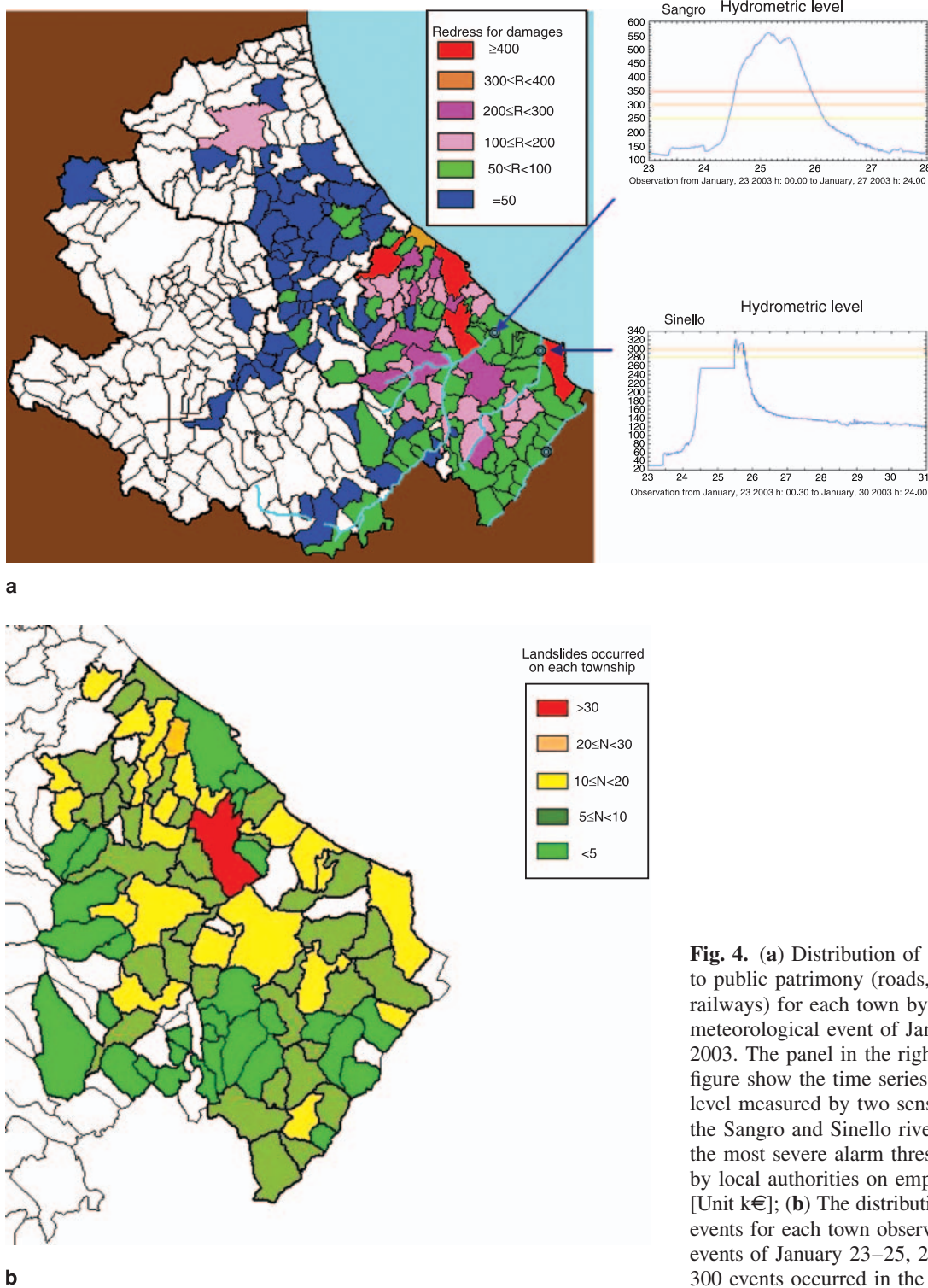


Fig. 4. (a) Distribution of damages caused to public patrimony (roads, bridges, railways) for each town by the sever meteorological event of January 23–25, 2003. The panel in the right column of the figure show the time series of hydrometric level measured by two sensor located along the Sangro and Sinello river, the red line is the most severe alarm threshold established by local authorities on empirical base [Unit k€]; (b) The distribution of landslide events for each town observed after the sever events of January 23–25, 2003. More than 300 events occurred in the selected area

of Euros, mostly in the Southeast Abruzzo region, a map of such damages for each township is given in Fig. 4a. A local authority unfortunately died during a rescue operation. The panels in the right column of Fig. 4a show the time series

of hydrometric level measured by two sensor located along the Sangro and Sinello river. The different lines correspond to different level of alarm threshold established by local authorities on empirical base.

3.2 Available data

Available data can be categorized with respect to type and source. During the event we can list the following sets:

- Visible (VIS) and infrared (IR) radiance maps have been provided by Meteosat-7 over areas of Southern Europe (e.g., Rivolta et al. 2006). The IR Meteosat-7 images considered here are composed by 547×298 pixels, corresponding roughly to longitudes ranging from 0 to 22° E and latitudes ranging from 36 to 48° N. Each pixel can be approximated as a square of 5×5 km 2 .
- Microwave (MW) radiance maps have been provided by the Special Sensor Microwave Imager (SSM/I) twice a day along the entire event (e.g., Ferraro 1997; Pierdicca et al. 2004). The SSM/I microwave radiometer operates on the DMSP satellites. It has four frequencies at 19.3, 22.2, 37.0, and 85.5 GHz with dual polarization, except the 22.2 GHz frequency, which works on vertical polarization only. It has a conical scan and a swath of 1400 km. On each scan, it takes 128 uniformly spaced samples at the 85 GHz frequency with a spatial resolution of 12.5 km. The others frequencies at 19.3, 22.2, and 37.0 GHz are sampled with a selected temporal and spatial resolution, i.e., 8.4 ms and 25 km (Hollinger et al. 1990).
- Reflectivity volume data have not been unfortunately available during the event due to a failure of the Abruzzo C-Band Doppler radar (Marzano et al. 2004b). Doppler moment profiles have been available from the Abruzzo wind profiler located in L'Aquila (Bianco et al. 2005).
- Hourly rainfall depth have been available from the rain gauge network of Abruzzo and Molise regions (Tomassetti et al. 2005). The network has a fairly high density with an average distance of about 20 km between rain gauges, which becomes smaller within mountainous regions. Similar data have been collected for Northern Italy.
- Radiosonde data of the main Italian stations have been available during the event together with the meteorological analysis of the European Centre for Medium-range Weather Forecast (ECMWF).

4. Remote sensing data processing

The problem of using satellite remote sensing data to retrieve rainfall is fairly complicated for several reasons. One reason is that presently there is not a single spaceborne platform which can carry all the suitable instruments to ensure the suitable properties to the rainfall product (Levizzani et al. 1996; Vicente et al. 1998; Turk et al. 2000; Marzano et al. 2001). From a meteorological point of view, visible and infrared radiometers can give information on cloud top layers. On the other hand, microwave radiometers can detect cloud structure and rain rate since MW brightness temperatures (BTs) are fairly sensitive to liquid and ice hydrometeors (Ferraro 1997; Bennartz and Petty 2001). Regarding platforms, Geosynchronous Earth Orbit (GEO) satellites can ensure coverage with a high temporal sampling, while Low Earth Orbit (LEO) satellites have the advantage to enable the use of microwave sensors, but with a major drawback of low temporal sampling. Therefore, LEO-MW and GEO-IR radiometry are clearly complementary for monitoring the Earth's atmosphere and a highly variable phenomenon such as precipitation.

Statistical integration of satellite infrared and microwave data can be accomplished in several ways (Kummerow and Giglio 1995; Bellerby et al. 2000; Marzano et al. 2001; Miller et al. 2001). One can resort to approaches whose aim is to combine IR measurements and MW-based estimates on a cumulative statistical distribution basis. Indeed, artificial neural network (ANN) can be also conveniently applied to the same problem dealing with empirically-trained algorithms showing comparable performances (Hsu et al. 1997; Grimes et al. 2003; Tapiador et al. 2004a, b; Coppola et al. 2006).

4.1 Satellite rainfall estimation

Neural networks present several advantages with respect to conventional statistical techniques (Tapiador et al. 2004a, b; Marzano et al. 2005). Their main feature is the ability to map input data to output data to any degree of non-linearity. It is well known that ANNs exhibit the capacity to learn and to represent highly non-linear functional.

Within the CETEMPS forecast chain, an Elman ANN system has been trained with space-time co-located infra-red (IR) and microwave data from SSM/I. Elman ANN (Elman 1990; Hecht-Nielsen 1991) is a multilayer network for which the status of neurons in the intermediate layer (usually referred as *hidden* layer) is propagated back to the input layer. The METEOSAT IR measurements from geostationary satellite have been co-located for a time step closer in time to the SSM/I pixel measurement from polar orbiting satellite. Rainfall estimates from SSM/I have been obtained using the algorithm of Ferraro et al. (1997). Both data sets refer to the European Mediterranean region for the period from 4:12 to 18:58 UTC of the 24 January 2003 for only 15 polar orbiting satellite passages.

Note that, since spatial resolution of microwave (MW) data is generally worse than IR ones, a MW field-of-view generally includes more than one IR pixel. For this reason a square grid with pixels of about 5×5 km has been used as NN

inputs for each cycle plus one more input containing the information of the elevation of the land surface given by a Digital Elevation Model (DEM). Those inputs have been calibrated with the rainfall value estimated for the SSM/I pixel in two different steps.

In the first step of the calibration the ANN algorithm is trained for giving an output of rain/no rain flags (i.e., a rain mask). This means that having in input the IR brightness temperature (BT) and the DEM information, the requested output is a rain mask. In the second step of the calibration the output of the previous ANN becomes the input of a second ANN and only for those pixels that are recognized as "wet" pixels the second ANN is trained to give the actual rainfall estimation using as input the rainfall mask, the BT map and the DEM map. The final ANN output is the rainfall map as it is shown in panel (b) of Fig. 5.

In Fig. 5, the results for the case study of the 23–25 January 2003 are shown. During this pe-

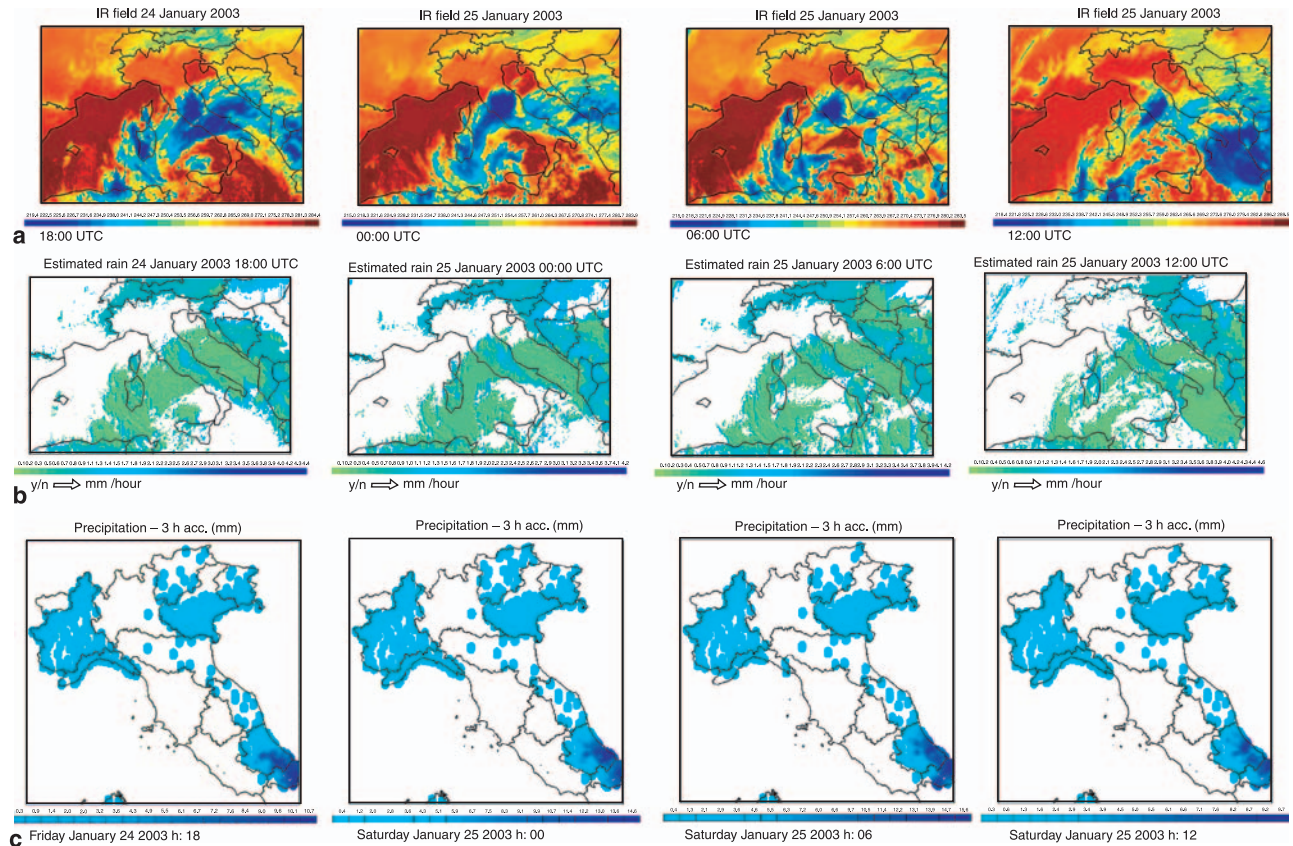


Fig. 5. (a) Shows METEOSAT IR on January 24 and January 25, sampled every 6 hours, (b) shows rainfall estimates by NEREMIS, and (c) shows raingauge map at the same time steps

riod the development of the intense cyclonic system over the Mediterranean area was observed and in the central part of the period a deep convective cell was localized over the Tuscany region in central western Italy and intense and persistent precipitation was observed in the Abruzzo region within Central Eastern Italy. In the first row a sequence of METEOSAT IR images is reported one every 6 hours from 24 January 18:00 UTC to 25 January 12:00 UTC. In the second row the corresponding rainfall estimation by NEREMIS (Neural Rainfall Estimation from Microwave and Infrared Sensors) is reported at a space resolution of $5 \times 5 \text{ km}^2$. The shape of the rainfall fields well corresponds to the BT maps for all the time steps and it describes in a fairly good way the different phases of the perturbation's development. In the third row gauge rainfall observations accumulated over a 3 hours period are reported for the same time step. It is interesting to notice how during the 23rd of January the rainfall was observed first over Sardinian island, later over the northeastern cost of Italy (Marche region) and at the end of the day the perturbation reached the Abruzzo region (not shown). During the 24th and 25th of January the synoptic configuration remains stable and the 26th of January the perturbation is resolving (not shown). The whole cycle described by the observations is well visible in NEREMIS rainfall fields, too.

4.2 Rainfall satellite nowcasting and radar retrieval

In this section, we highlight two remote sensing techniques which were not applied in the analysis of this specific case, but are integral part of the remote sensing package within the CETEMPS forecast chain. These two methodologies refer to: (i) satellite nowcasting; (ii) radar retrieval.

For civil protection purposes, short-term prediction of rain fields may be essential to forecast ground effects. The following nowcasting methods may be classified among standard, or in this paper “conventional”, techniques: (i) persistence method, which assumes that each pixel in the forecasted satellite image is associated to the same value as in the previous image; (ii) steady-state method, which assumes that the structures in the image are advected but unchanged in size

and intensity (the forecasted image is the latest available satellite image translated by a suitable motion vector); (iii) linear method, consisting in linearly extrapolating the future value of a pixel in the satellite frame from the latest two values available. Each of these conventional nowcasting methods shows a performance that depends on the weather conditions in the considered region and on the space-time scale of integration of the rainfall field. None of the three can be assumed as the best method for all possible conditions. In general, ANNs provide a powerful methodology to predict temporal series of random variables. Within the CETEMPS chain, it has been also implemented a ANN-based nowcasting algorithm (Rivolta et al. 2006). ANNs have been trained to forecast the IR temperature value associated to a certain pixel of the satellite image, starting from the measured values in a region around that pixel in the previous satellite images. To this aim, a great number (some tens of thousands) of input pattern/target pairs are provided to the network during the training phase. The neural nowcasting technique proposed here has been based on the feedforward multi-layer structure.

The Abruzzo meteorological radar was installed in the Abruzzo region near L'Aquila (Italy) on November 1997 and operated by CETEMPS in Central Italy in the middle of Apennine mountain range extending along the length of the Italian peninsula (Marzano et al. 2004b). The horizontally-polarized radar is placed on a 10-m height tower, having a radome-covered parabolic antenna of 2.44-m diameter, a 1.6° half-power beam-width and 40-dB directivity. The magnetron peak-power is 250 kW at 5.6 GHz with a pulse repetition frequency (PRF) of 250 Hz (i.e., intensity mode with a pulse width of 1.98 μs) and 787, 885 and 1180 Hz (i.e., velocity mode with unfolding option and a pulse width of 0.75 μs). The receiver sensitivity is -110 dBm . The maximum range is 480 km and 120 km for the intensity and velocity mode, respectively. During the acquisition mode, a uniform angular resolution of 1° for both elevation (up to 7°) and azimuth angles is maintained constant without changing the pulse duration. Self-contained software is used to remotely operate and archive radar data. The block diagram of the overall radar retrieval algorithm is illustrated in Marzano et al. (2004b). De-cluttering is of particular import-

tance in complex topography. We have adopted a scheme based on the construction of an areal clutter map. The latter is obtained by averaging, for each range gate, the reflectivity measurement in clear-air conditions. This scheme has been integrated with spectral and statistical signal processing, routinely performed using signal temporal autocorrelation, histogram and Doppler velocity analysis. Classification of rain events into stratiform and convective regimes is carried out by using a reflectivity horizontal gradient and intensity technique, tuned to the local climatological conditions (Montopoli et al. 2006). Significant path attenuation, due to convective rainfall, is possibly corrected by using an iterative forward algorithm applicable to polarimetric data as well (Vulpiani et al. 2005). In order to avoid instabilities, a check of convergence of the retrieved reflectivity range-profile is also performed. Even though procedures to remove the bright-band contamination are available, this correction is not generally accomplished within the retrieval algorithm since it is implicitly treated within the VPR reconstruction (Marzano et al. 2004b). Rainfall fields, derived from C-band radar and averaged to 500 m, are finally input to the spatial integration tool, as indicated in Fig. 1.

5. Meteorological modelling and forecast

In the next two paragraphs a brief overview of the high-resolution model and the analysis of forecasted rain fields will be discussed.

5.1 Mesoscale numerical model

The MM5 mesoscale model (Dudhia 1993; Grell et al. 1994) from Penn State University and National Centre for Atmospheric Research (PSU/NCAR) is used operationally at CETEMPS. The model configuration used in this work is similar to the operational one, the main difference being in the numbers of the nested domains. In this case study, 4 domains are used to enhance the resolution up to 1 km on the target area. Therefore, the following configuration is used: the model is running with 29 vertical levels, 27 km of grid step in region lat. = [35°, 50°] – lon. = [-3°, 23°]; four domains two way nested are used, with a resolution of 27 km for domain

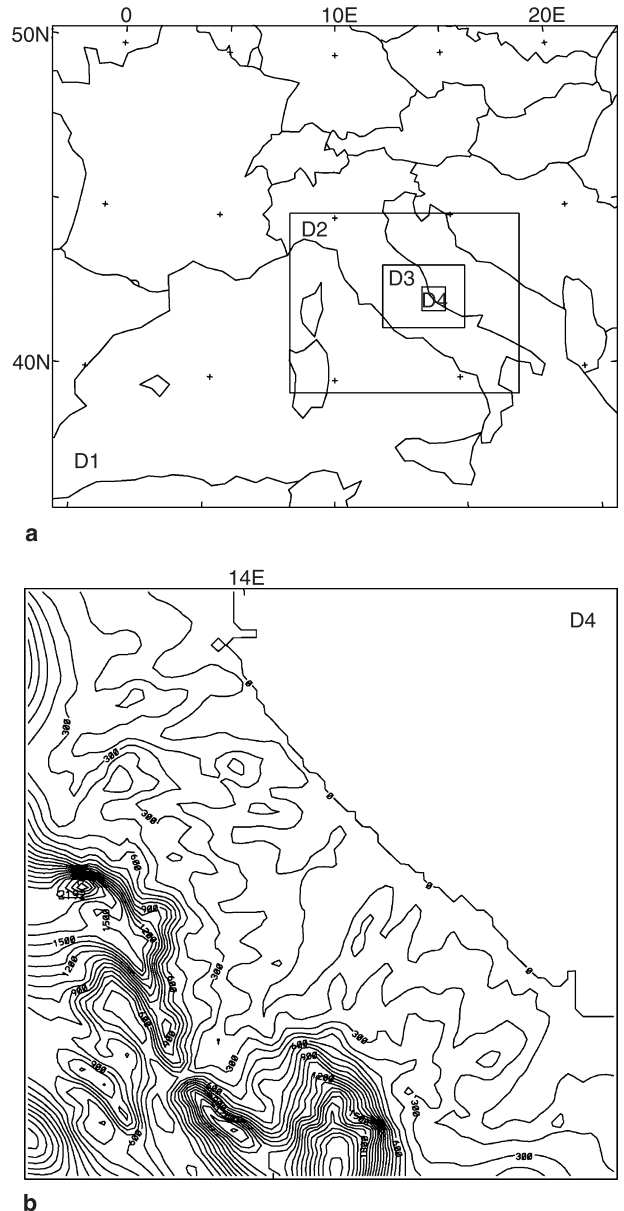


Fig. 6. Model domains (a) and topography for domain 4 (b) (contour interval = 100 m)

1, 9 km for domain 2, 3 km for domain 3 and 1 km for domain 4 (Fig. 6).

The Troen and Mahrt (1986) parameterization for the PBL is used associated to the Kain and Fritsch (1990) parameterization for the cumulus convection. An explicit scheme for the micro-physics (R1) is also used (Reisner et al. 1998). This scheme accounts for cloud water (q_w), cloud ice (q_i), rain (q_r) and snow (q_s) to be produced simultaneously, but it does not account for the production of graupel. The dimensional distribution of the hydrometeors is assumed to follow

the Marshall–Palmer distribution (Marshall and Palmer 1948)

$$N_h dx = N_h^0 e^{-\lambda x} dx, \quad (1)$$

where x is the particle size, h is a generic hydrometeor, λ is the slope parameter and N_h^0 is the intercept parameter. λ is inversely proportional to the mixing ratio of each hydrometeor ($q_h \equiv q_w, q_i, q_r, q_s$):

$$\lambda = \left(\frac{\pi \rho_h N_h^0}{\rho q_h} \right)^{1/4}, \quad (2)$$

where ρ is the density of air and ρ_h is the density of hydrometeors. That is: the greater the mixing ratio, the wider is the size distribution. The intercept parameters N_h^0 are fixed for the R1 scheme

(Reisner et al. 1998). The model simulations are initialized using ECMWF data analyses.

5.2 Forecasted rainfall

The analysis of the forecast rainfall is performed on the high resolution domain (at 1 km). Assessments on the improvements of the rainfall prediction using high resolution models are behind the aim of this paper, for discussion on the topic see (Ferretti et al. 2003a).

The 6-hour accumulated precipitation at two different time steps (January 24 at 1200 UTC and 25 January at 0600 UTC) is analyzed. During January 24, the MM5 clearly reproduces the spiral structure of the precipitation (Fig. 7a) associ-

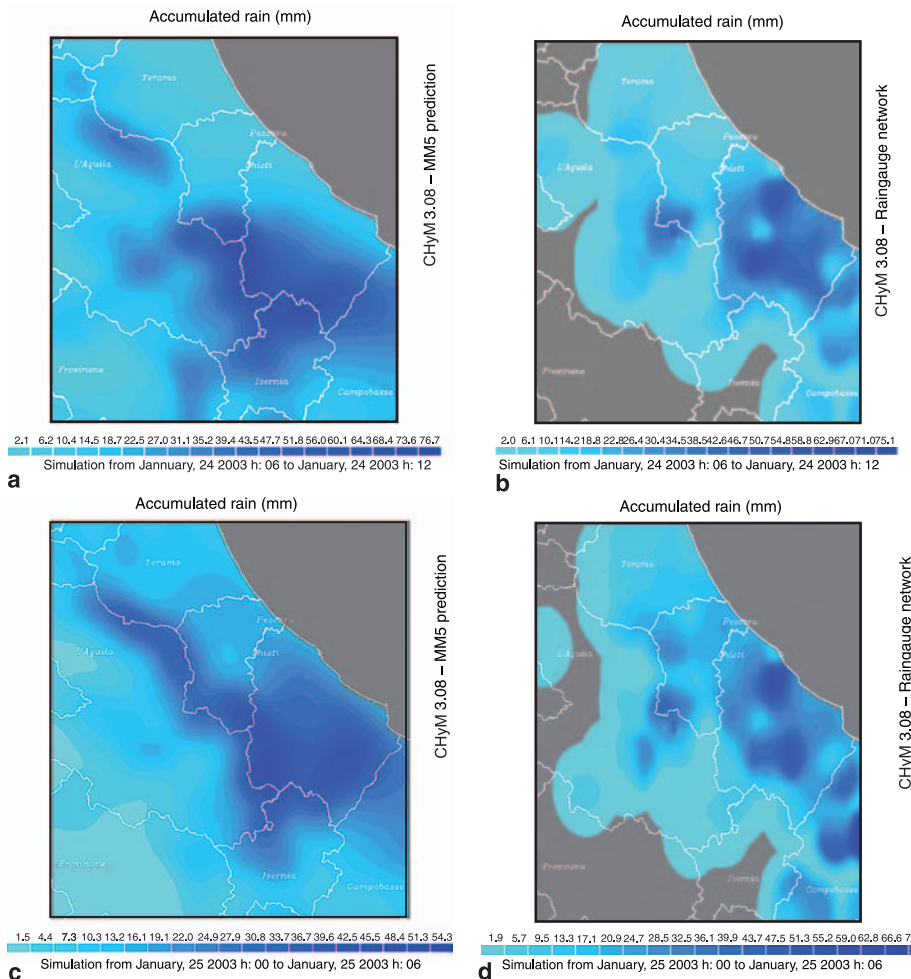


Fig. 7. 6-hours accumulated precipitation ending at 12:00 UTC on January 24 as predicted by MM5 (upper left panel) and rebuilt from rain gauge observations (upper right panel). Lower panels show the same but for 6-hours accumulated precipitation ending at 06:00 UTC on January 25. All these precipitation fields were rebuilt using CHyM hydrological model routines and then the precipitation field is not rebuilt (grey zones) on the sea zone or where observation are not available

ated to the surface depression as observed by the satellite (Fig. 5a), but a generalized underestimation of the precipitation is found. In fact, maxima of rainfall (Fig. 7a, b) are produced only along the mountain ridges (associated to the spiral structure) confirming the MM5 tendency to produce precipitation on the windward side of the mountains (Ferretti et al. 2003b; Colle et al. 2005; Serafin and Ferretti 2007); moreover, the Northward displacement of these maxima (Fig. 7a) with respect to the observations (Fig. 7b) confirms the MM5 tendency to anticipate meteorological systems (Ferretti and Faccani 2005). Furthermore, the large underestimation of rainfall in South Abruzzo (along the coast, Fig. 7a, b) where peaks of the rainfall intensity (up to 45 mm/h) were recorded, clearly suggests that MM5 is missing the convective precipitation. Indeed, convective rainfall embedded in the frontal system are inferred by the lightning recorded between 00 and 02 UTC (Fig. 3a) in this area. During January 25, rainfall is slightly reduced (Fig. 7d), as the residual lightning recorded between 0500 and 0800 UTC confirms (Fig. 3b), but it is still observed in the same area. This suggests a persistency of the rainfall that would motivate the heavy damages produced by this event. In fact, a flood may be produced either by a large amount of rainfall or by the time of the rainfall to cross the area, or by a combination of both of them, as Rotunno and Ferretti (2001) showed for the Piedmont flood 1999. In this case, the rainfall produced by MM5 (at this time step) suggests a rapid evolution of the system, and the large underestimation of the rainfall (Fig. 7c) confirms it. Beside from this underestimation of the rainfall, MM5 shows a good agreement in the location of the maximum rainfall along the mountain ridge and close to the coast in the south of Abruzzo, and, as it will be shown in the next paragraphs, this high resolution forecast is a good support for mapping the alert.

Finally, the MM5 shortcomings in the rainfall forecast are well known and several techniques are applied to overcome these problems: assimilations of local data to reduce the time delay or predate (Ferretti and Faccani 2005) and improve the rainfall, and tuning of the microphysical parameters to improve both the location and the amount of rainfall (Colle et al. 2005; Garvert et al. 2005; Serafin and Ferretti 2007). These methods will be both further investigated and applied to this case.

6. Hydrological numerical modelling

The CETEMPS HYdrological Model (CHyM) is a grid based distributed model that can be run in any geographical domain and with any resolution up to the resolution of the implemented Digital Elevation Model (DEM), i.e. about 300 m (Coppola et al. 2007; Tomassetti et al. 2005). For operational purpose the capability to simulate an arbitrary domain corresponds to the need to run the model for those river basins that are more stressed by the current meteorological events. CHyM model simulates the physical processes contributing to the hydrological cycle using an approach similar to other models (see, as an example, Borah et al. 2002; Todini and Ciarrapica 2002). Based on the kinematic wave approximation of the shallow water wave (Lighthill and Whitam 1995) the surface routing overland and channel flow are simulated solving the continuity and momentum conservation equations:

$$\frac{\partial A}{\partial t} + \frac{\partial Q}{\partial x} = q, \quad (3)$$

$$Q = \alpha A^m, \quad (4)$$

being A the flow cross-sectional area, Q the flow rate of water discharge, q the rate of lateral inflow per unit of length, t the time, x the coordinate along the river path. α is the kinematic wave parameter and m is the kinematic wave exponent. The potential evapotranspiration is computed using the Thornthwaite formula (Todini 1996; Thornthwaite and Mather 1957). The infiltration process is modelled using a conceptual model similar to those proposed by several authors as Overton (1964) and Singh and Yu (1990). A more complete description of the model is beyond the scope of this paper and we only discuss a few aspects that are relevant for the application described in this paper.

The extraction of a coherent flow scheme is a fundamental step to simulate the hydrological cycle for a given geographical domain. In many distributed and lumped hydrological models (Singh and Frevert 2002), stream network is usually extracted using commercial or free Geographic Information System (GIS) software, however this “automatic” approach could cause an unrealistic modification of DEM or the algorithm could be too simple and not suitable for

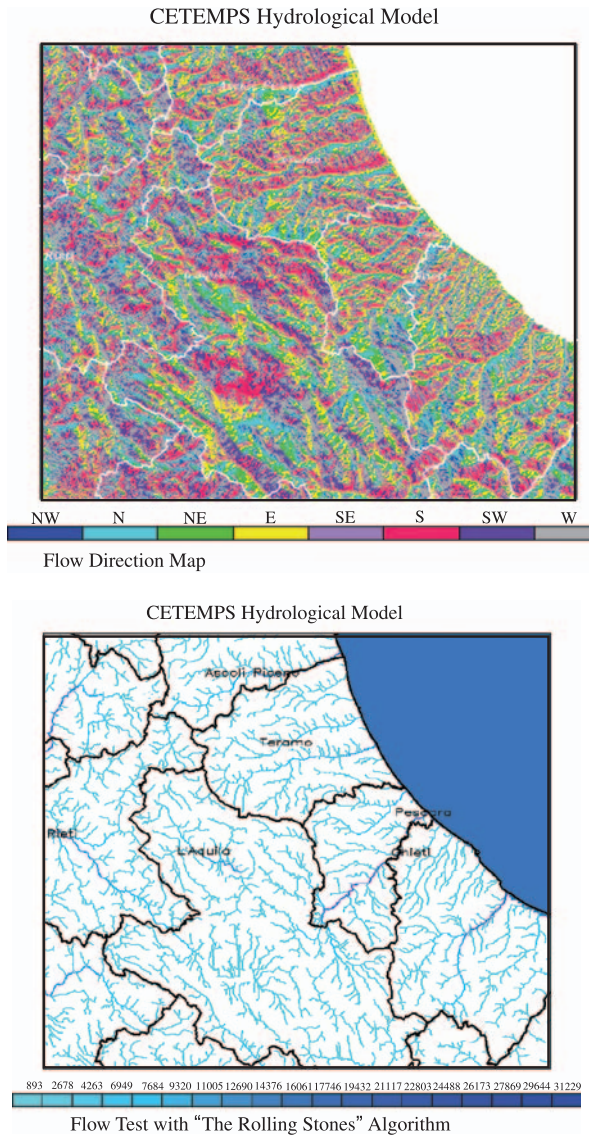


Fig. 8. CHyM flow direction maps (upper panel) and drainage network (lower panel) over the Abruzzo region. In upper panel each grid point of domain is characterized by 1 of 8 different color each representing the flow direction for that cell (from Northwest to West). In the lower panel the drainage network is rebuilt calculating the accumulation matrix, i.e., for each cells the total number of drained cells

a realistic hydrological reconstruction of an arbitrary catchment. For a distributed grid based model the first step to obtained the drainage network shown in the lower panel of Fig. 8, consists in the definition, for each grid point, of the runoff flow direction. According to the principle of minimum energy, it is usually assumed that surface runoff occur with a strong preferential direction following steepest DEM downhill

gradient. Unfortunately the application of this algorithm is not trivial because of the occurrence of singularities due to the finite horizontal and vertical DEM resolution. These singularities are usually classified as “pits” and “flat areas”. The pits (or sinks) are DEM cells surrounded by neighbours that have higher elevation. In most of GIS software and other hydrological models, the sinks are removed increasing the DEM value to the lowest elevation of the adjacent cells, this technique is usually referred as filling algorithm (Martz and Garbrecht 1992, 1993; Band 1986). It is easy to understand how this algorithm often simply moves the pit in one of neighbouring cells, therefore the procedure must be applied several times and it can lead to an unrealistic modification of DEM. The flat areas are sequences of adjacent cells having a slightly different elevation. In this case a more sophisticated numerical procedure is requested to coherently establish the flow direction for the whole flat surface; examples of such strategies are described by Turcotte et al. (2001) and Garbrecht and Martz (1997). CHyM model implements an original and sophisticated technique to filter the DEM singularities. The algorithm, called CA2CHyM, is essentially based on the main concept of Cellular Automata (CA) theory (Packard and Wolfram 1985). A complete description of CA based approach to smooth DEM is reported in Coppola et al. (2007) and can be quickly resumed as following:

- CHyM grid is considered an aggregate of cellular automata;
- The status of a cell corresponds to the value of a CHyM field (DEM, in this case);
- The state of the cells in the lattice is updated according to following rule

$$h_i \rightarrow h_i + \alpha \left(\sum_j^8 \beta_j (h_j - h_i) \right), \quad (5)$$

being h_i the height of cell i ;

- All the cells of the lattice are updated synchronously;
- Update ends when the flow direction can be established for all the cells.

In Eq. (5), the α coefficient is a small value (typically 0.1), while the coefficients β_j are weights taking into account the different dis-

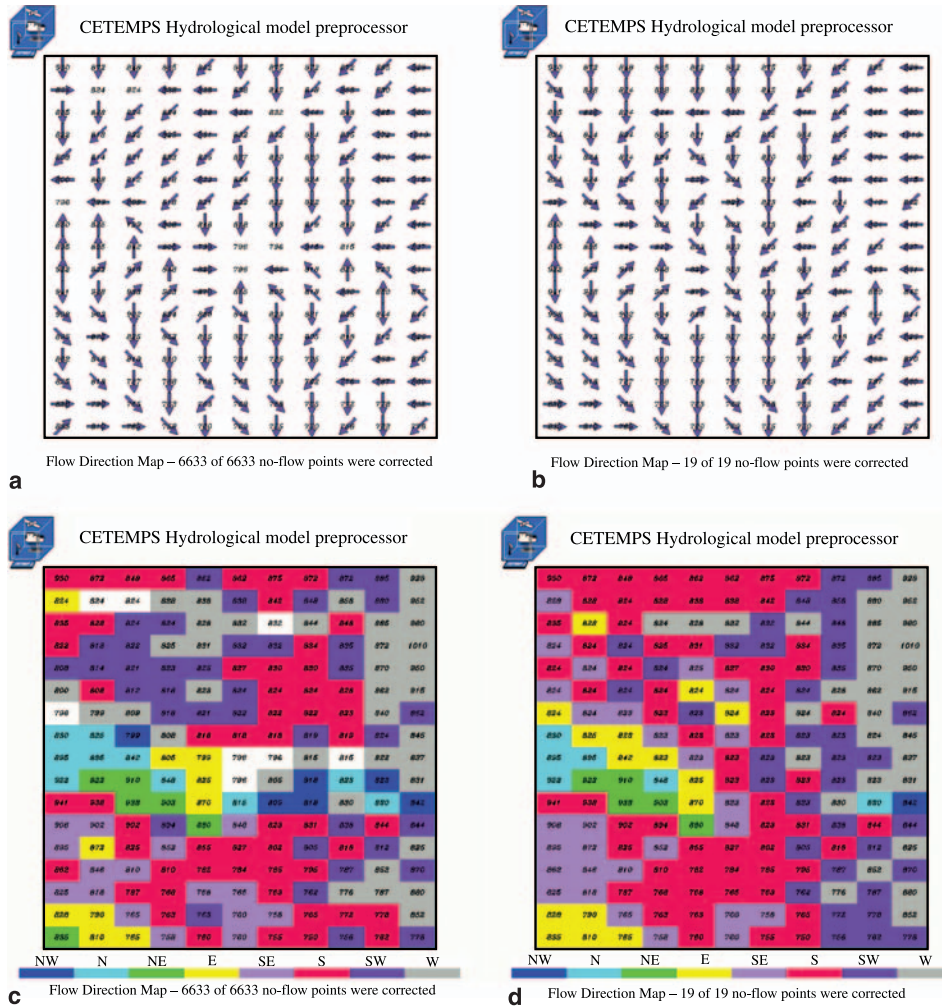


Fig. 9. Example of cell over flats area or pits where the flow direction is established by means of Cellular Automata algorithm. (a, c) Show example of cells where the flow direction cannot be established (no arrow and white color respectively); (b, d) show how the singularities disappear after the application of the CA based algorithm

tances between the centre of the cells; the sum is carried out on the 8 surrounding cells.

An example of the application of this technique for a small subdomain is given in Fig. 9. The upper left panel shows as for few grid points it is not possible to establish the flow direction because of the presence of pits or flat areas. In the upper right panel these singularities are solved by the application of CA based algorithm. The lower panels show the same but in this case the flow direction is indicated by different colors. It is important to note as the technique leads not only to the definition of the flow direction for grid points where singularities occur, but also the flow direction in the surrounding cells are coherently changed.

7. Flood alert mapping

In the following paragraphs we will focus on data integration within the CETEMPS forecast chain, as shown in a schematic view in Fig. 1, as a final step for producing a flood alert map, defined a given quantitative criterion of flood danger.

7.1 Data integration

A CA-based algorithm discussed in the previous section is also used for rainfall modelling to represent the essential aspect of spatial rainfall patterns merging rain information from different data sources (Tomassetti et al. 2005; Coppola et al. 2007). The aim of the algorithm is to down-scale the precipitation field to a typical hydrolog-

ical model resolution and for this purpose it combines all the available rain data: observed, estimated and simulated. The different sources are combined accounting for the nature of the data. The basic idea dealing with hydrological model at resolutions of few hundreds of meters, is to consider that the rainfall at a given grid point is given by the weighted average of the precipitation in the surrounding cells, with the weights depending on the distances between the grid points. The CA based algorithm essentially acts to find a coherent solution considering the precipitation at each grid cell as the weighted average of the precipitation in the neighbourhood. In order to explain few details of this technique, we can consider a domain that represent our watershed and on which it is defined a grid of a fixed resolution. The goal is to assimilate a data set that consists of hourly rainfall observations onto a sparse grid. Each CHyM grid point is then defined by a different type. Cells of Type 0 are those for which there is little interest in estimating the precipitation, for example, because they are points corresponding to the sea or they are located outside the catchment of interest. The cells of Type 1 are grid points for which we do not yet

have a precipitation estimate. Cells of Type 2 are those for which the precipitation has been estimated in a previous module with a different data set and this precipitation value will not change with the application of subsequent modules.

In the grid points that correspond exactly to the location of the raingauges that are to be assimilated in the present module, the value of the precipitation is set to the value of the corresponding observation and they are from now on considered of Type 2 (the value of the precipitation will not be changed any more). The cells of Type 3 correspond to all the cells whose precipitation value will be established within the current module and, this sub-domain is represented by all the cells having at least a measurement in a selected radius of influence r_m of the actual rain measure or estimate. The next step is to use a CA-based algorithm similar to that described above for the DEM smoothing, for establishing a coherent value for the grid points of Type 3. As shown in Coppola et al. (2007) the iteration of this CA based algorithm allows to obtain a reconstruction of complex precipitation pattern resulting more realistic with respect to the one obtained with a simple geometrical interpolations. An ex-

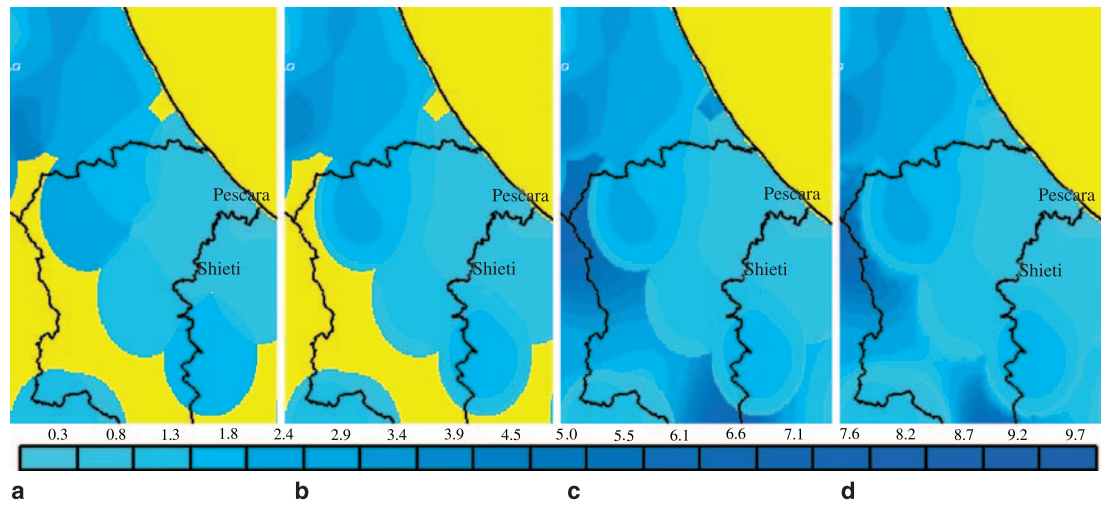


Fig. 10. Rainfall data integration as performed by CHyM model with the Cellular Automata based algorithm. The sequence of panels shows how the rainfall fields (mm) is rebuilt using different data set. In the first panel raingauges network has been used and the precipitation at each grid point is rebuilt as the weighted average of the closest available measurements, the yellow zone corresponds to the subdomain where no measurements are available. In the second panel the CA algorithm has been applied and the two dimension field is smoothed. It has to be noted the ability of the proposed technique to rebuild a more realistic precipitation fields (second panel) respect to a simple geometric algorithm (first panel) whose pattern is similar to a superimposition of circles. In the third and fourth panels the same technique is used to acquire precipitation forecast where no raingauges are available. Rainfall data integration as performed by CHyM by means of Cellular Automata algorithm. (a) Raingauge; (b) smoothed raingauge; (c) raingauge + MM5 data; (d) raingauge + smoothed MM5 data

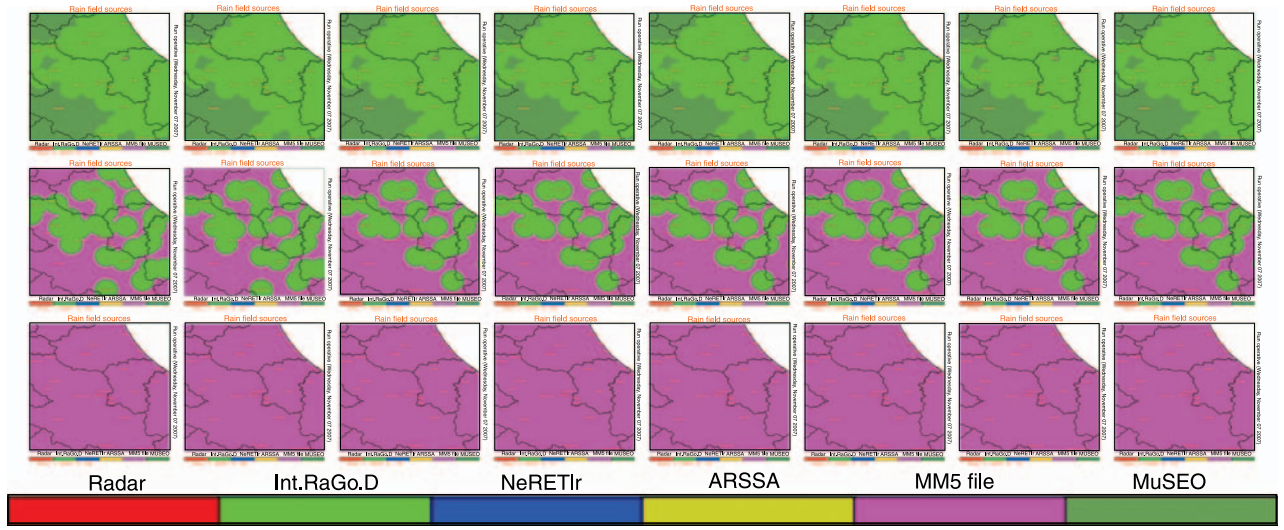


Fig. 11. An example of rainfall data integration and rain field rebuilt as performed by CHyM for operational activities. Each map represents the different sources used to rebuild the precipitation field at each hour (from left to right and from high to low). In the first row (many hours before the start of simulation) the light green color locate the subdomain where the raingauge observations have been used and the dark green shows the subdomain where rainfall values were retrieved from the MM5 simulation of the past days (from a data base called MuSEO). In the second row (few hours before the simulation) the pink color shows the subdomain where the MM5 quantitative rainfall predictions have been used while the light green color locate the subdomain where the observations are already available. Of course from the third row (future hours) only the MM5 precipitation predictions are available

ample of the application of this algorithm is shown in Fig. 10.

An example of the sequence of rainfall data sources used by CHyM hydrological model during operational activities to rebuilt the precipitation field at different time steps is shown in the sequence of map of Fig 11. Each map shows the situation for one hour of integration and different colors correspond to different data sources. Pink color locates the subdomain where MM5 model forecast have been used, green color locates the subdomain where rain gauges measurements are available. The simulation shown in Fig. 11 was carried out at 8 am of August, 25 2005, for the previous day the rainfall spatial distribution is rebuilt using the raingauge network. For the hours ranging from 0 am to 6 am of August, 25 only few raingauge measurements are available and a part of rainfall space pattern is rebuilt using MM5 model forecast. Of course for “future” time steps only meteorological prediction are available.

7.2 Flood alerting

In real time operational work an alert system is often required. From an hydrological point of view to estimate the possibility that a region is

affected by a flood would be of great advantage because we could focus accurate simulation in the most probable flood region saving time and computer resources.

Moreover the possibility to have a realistic map of flooding risk could be a crucial information for the risk management activities carried out by the civil protection and local authorities. We will show in this paragraphs as the drainage network extraction technique implemented in the CHyM model and an accurate reconstruction of precipitation field at hydrological scale are sufficient to provide a flood alarm index that is able, at least in the case studies discussed here and in Tomassetti et al. (2005) to localize the segments of drainage network where flood events are more likely to occur.

The use of a distributed hydrological model for the prediction of flow discharge requires a complex calibration activity. In addition only few complete discharge time series are available for numerical models validation while these time series are usually missing for small catchments. In a region of complex topography, like the Central Italy where CHyM model is used at present time, is therefore very difficult to validate a deterministic prediction of flow discharge for tens of small basins. A more empirical but realistic approach

could be the use of a stress index as an estimator of the probability that a certain segment of the simulated drainage network is undergoing to a flood. As a first simple approach this kind of index can be derived as a function of the rainfall drained by an elementary cell of the simulated domain and the hydraulic characteristic of the draining channel within that cell. The cross section of the river is usually considered, as a first approximation, a linear function of the total drained area (Borah et al. 2002) and therefore a reasonable idea could be to consider the ratio between the total drained rain and total drained area in the upstream basin of each cell. More specifically the CHyM stress index SI for the cell k can be defined as follows:

$$SI_k = \frac{\sum_i \sum_j w_{ij}}{\sum_i \sum_j a_{ij}}, \quad (6)$$

where the sums over i and j includes all grid points in the upstream basin of the cell k , w_{ij} indicates the rain associated with the cell i,j and a_{ij} is the area of the cell i,j .

The total drained rain is calculated over a time range representing a typical runoff time for the considered basins, the runoff time is usually defined as an average time that a drop of rain will take to runoff toward the sea. A time interval of 48 hours has been chosen for the case studies discussed by Tomassetti et al. (2005) and the same interval has also been used for the application of the SI to the case study of 23–25 January 2003 and illustrated in Fig. 12 where the Stress Index simulated in operational condition is plotted for three different scenarios.

The SI obtained from the satellite rain estimates is clearly underestimating the flood event (panel *a*), but the segment of drainage network where the major flood events occurred are correctly located. Panels *b* and *c* show the alarm map when the stress index is computed operationally (e.g., when only the MM5 forecast is available) and when the gauge observations are available, too. The intensity of stress is correctly detected by the proposed algorithm although the location is slightly shifted towards the inner part of the domain.

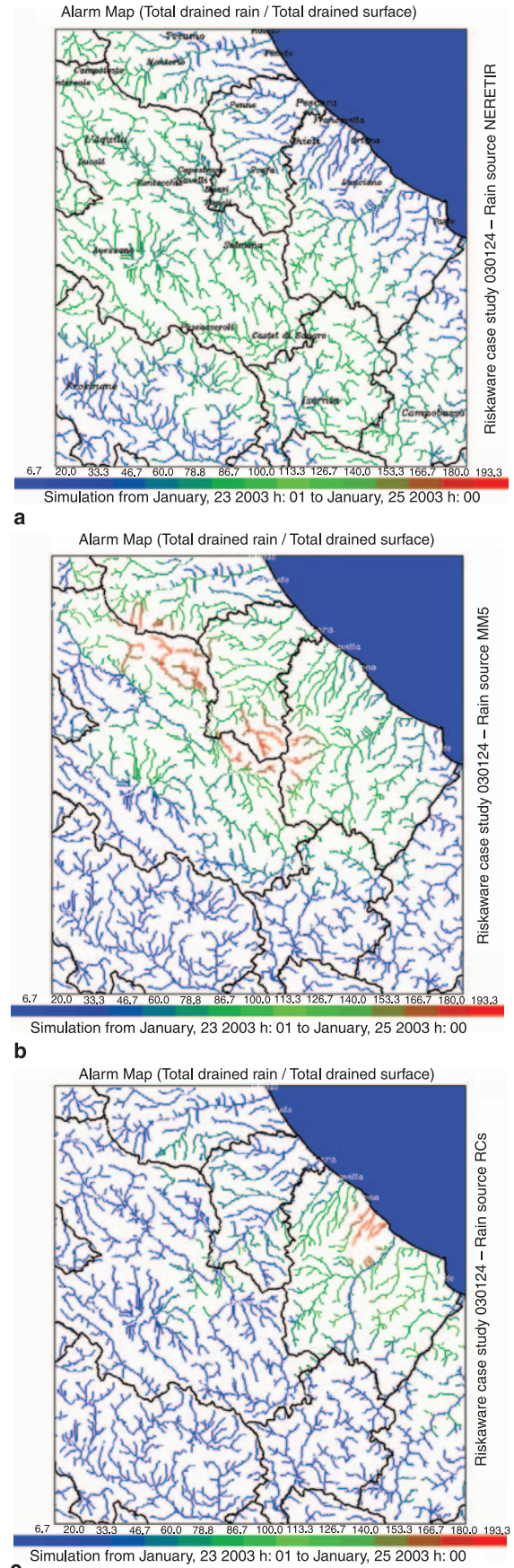


Fig. 12. Alert maps as derived by CHyM from: (a) from satellite retrieved rain fields; (b) from MM5 forecasted rain fields; (c) from rain gauge mapped rain data

8. Conclusions

A flood forecast chain, developed at the Centre of Excellence for Remote Sensing and Hydro-Meteorology Modelling (CETEMPS) and based on coupled mesoscale atmospheric model and a distributed geomorphological routing scheme with in-situ and remote sensing data integration, has been illustrated. The focus has been on small-catchment flood forecast in complex orography in Central Italy, but the developed modelling and processing integrated tools may be easily applied to any geographical and orographic scenario.

Emphasis has been put on the integration of numerical models and retrieval algorithms with aim to provide an overview of an objective system for hydro-meteorological alert-map emission. The possibility to acquire different rainfall data sources during operational activities has also been stressed and a quick description of CA based algorithm to merge different observations, estimation and meteorological prediction has also been given. As an example, the forecast hydro-meteorological chain have been applied to a case study of an extreme event occurred on 23–25 January 2003 and results have been discussed. We suggested to use an empirical stress index to provide a simple and efficient method to locate the small basin or the parts of the simulated catchments undergoing to major hydrological stress. The proposed CHyM stress index has also a simple physical interpretation: it represents the average precipitation for the upstream basin of a cell in the considered time interval. It is also important to note as the CHyM stress index is calculated making a sort of spatial (all the upstream basin) and temporal (runoff time) average and this reduce the effect of different uncertainties in the reconstruction of rainfall fields from observation and/or meteorological forecast. Of course the most important reason to support the definition of such index is the observation that it actually seems to be a powerful method to localize the segments of drainage network where flood events actually occurred. The quantitative analysis of different case studies corroborates the hypothesis that 200 mm of precipitation in the upstream basin in a time interval comparable with the runoff time of the river seems to be a reasonable threshold to predict possible hydrological risk.

The successful example showed in this paper is not a single case study. The CETEMPS forecast chain is routinely operated every day and its outputs can be visible at: <http://cetemps.aquila.infn.it>. These outputs are operationally used within the Civil Protection office of the Abruzzo region in Italy. The analysis of several case studies has also proved the fact that the accuracy of hydrological prediction becomes worse and worse as the data sources ingested become more sparse and poorer in quality. On the other hand, the need of coupling in consistent and robust way both meteorological and hydrological numerical models is essential for a physically-based forecast at very high spatial resolution in complex orography.

Acknowledgements

This work has been funded by the INTERREG III-B CADSES project RiskAWARE (2004–2006). Region Abruzzo, Italy and the Italian Ministry of Education, University and Research (MIUR) are also acknowledged for their partial support. The valid and continuous support of Dr. L. Bernardini and Dr. G. Cinque (Region Abruzzo and CETEMPS) within the operational activities is also kindly acknowledged. An overview of the case study data and the related analysis is available on-line at <http://cetemps.aquila.infn.it/riskaware>.

References

- Band LE (1986) Analysis and representation of drainage basin structure with digital elevation data. In: Proc. 2nd Int. Conf. on Spatial Data Handling, Int. Geogr. Union, Williamsville, New York, USA, pp. 437–50
- Bellerby T, Todd M, Kniveton D, Kidd C (2000) Rainfall estimation from a combination of TRMM precipitation radar and GOES multispectral satellite imagery through the use of an artificial neural network. *J Appl Meteor* 39: 2115–28
- Bennartz R, Petty GW (2001) The sensitivity of microwave remote sensing observations of precipitation to ice particle size distributions. *J Appl Met* 40: 345–64 (Jeffrey EL. Finding structure in time. *Cog Sci* 14: 179–211)
- Bianco L, Cimini D, Marzano FS, Ware R (2005) Combining microwave radiometer and wind profiler radar measurements for high-resolution atmospheric humidity profiling. *J Atmos Oceanic Tech* 2(7): 949–65
- Borah DK, Xia R, Bera M (2002) DWSM – A Dynamic Watershed Simulation Model. Mathematical Model for Small Watershed Hydrology, WRP Edition
- Bringi VN, Chandrasekar V (2001) Polarimetric Doppler weather radar: principles and applications. Cambridge University Press, Cambridge

- Bougeault P, Binder P, Buzzi A, Dirks R, Houze R, Kuettner J, Smith RB, Steinacker R, Volkert H (2001) The MAP special observing period. *Bull Amer Meteor Soc* 82: 433–62
- Buzzi A, Tibaldi S (1977) Inertial and frictional effects on rotating and stratified flow over topography. *Quart J Roy Meteor Soc* 103: 135–50
- Buzzi A, Tartaglione N, Malguzzi P (1998) Numerical simulations of the 1994 Piedmont flood: role of orography and moist processes. *Mon Wea Rev* 126: 2369–83
- Colle BA, Garvert MF, Wolfe JB, Mass CF, Woods CP (2005) The 13–14 December 2001 IMPROVE-2 event. Part III: simulated microphysical budgets and sensitivity studies. *J Atmos Sci* 62: 3535–58
- Coppola E, Grimes DIF, Verdecchia M, Visconti G (2006) Validation of improved TAMANN neural network for operational satellite-derived rainfall estimation in Africa. *J Appl Met* 45(11): 1557–72
- Coppola E, Tomassetti B, Mariotti L, Verdecchia M, Visconti G (2007) Cellular automata algorithms for drainage network extraction and rainfall data assimilation. *Hydrol Sci J* 52(3): 579–92
- Dudhia J (1993) A non hydrostatic version of the Penn State–NCAR mesoscale model: validation tests and simulation of an Atlantic cyclone and cold front. *Mon Wea Rev* 121: 1493–513
- Ebert EE, Janowiak JE, Kidd C (2007) Comparison of near-real-time precipitation estimates from satellite observations and numerical models. *Bull Am Met Soc* 88: 47–64
- Elman LJ (1990) Finding structure in time. *Cogn Sci* 14: 179–211
- Faccani C, Cimini D, Ferretti R, Marzano FS, Taramasso AC (2005) 3DVAR assimilation of SSM/I data over the sea for the IOP2 MAP case. *Adv Geosci* 2: 229–235
- Ferraro RR (1997) SSM/I derived global rainfall estimates for climatological applications. *J Geophys Res* 102: 16,715–35
- Ferretti R, Faccani C (2005) Data assimilation of high density observations: Part II. Impact on the forecast of the precipitation for the MAP/SOP IOP2b. *Q J R Meteorol Soc* 131A: 43–62
- Ferretti R, Paolucci T, Giuliani G, Cherubini T, Bernardini L, Visconti G (2003a) Evaluation of high resolution real-time forecast over the alpine region during MAP/SOP. *Q J R Meteorol Soc* 129B: 567
- Ferretti R, Paolucci T, Bernardini L, Visconti G (2003b) The role of the high resolution weather forecast in estimating the runoff using a simple hydrological model. *Ann Geophys* 46: 321–29
- Ferretti R, Faccani C, Cimini D, Marzano FS, Memmo A, Cucurull L, Paciòne R (2005) Simulations of deep convection in the Mediterranean area using 3DVAR of conventional and non-conventional data. *Adv Geosci* 2: 65–71
- Fornasiero A, Alberoni PP, Vulpiani G, Marzano FS (2005) Reconstruction of reflectivity vertical profiles and data quality control for C-band radar rainfall estimation. *Adv Geosci* 2: 209–15
- Garbrecht J, Martz LW (1997) The assignment of drainage direction over flat surfaces in raster digital elevation model. *J Hydrol* N 193: 204–13
- Garvert MF, Woods CP, Colle BA, Mass CF, Hobbs PV, Stoelinga MT, Wolfe JB (2005) The 13–14 December 2001 IMPROVE-2 event. Part II: comparison of MM5 model simulations of clouds and precipitation with observations. *J Atmos Sci* 62: 3520–34
- Grell GA, Dudhia J, Stauffer DR (1994) A Description of the Fifth-Generation Penn State/NCAR Mesoscale Model (MM5). NCAR Tech. Note NCAR/TN-398 + STR
- Grimes DIF, Coppola E, Verdecchia M, Visconti G (2003) A neural network approach to real time rainfall estimation for Africa using satellite data. *J Hydrometeor* 6(4): 1119–33
- Hecht-Nielsen R (1991) Neurocomputing. Addison Wesley
- Hollinger J, Peirce J, Poe G (1990) SSM/I instrument evaluation. *IEEE Trans Geosci Remote Sens* 28(5): 781–90
- Hsu KL, Gao X, Sorooshian S, Gupta HV (1997) Precipitation estimation from remotely sensed information using artificial neural networks. *J Appl Meteor* 36: 1176–90
- Kain JS, Fritsch JM (1990) A one-dimensional entraining/detraining plume model and its application in convective parameterization. *J Atmos Sci* 47: 2784–802
- Kummerow C, Giglio L (1995) A method for combining passive microwave and infrared rainfall observations. *J Atmos Oceanic Technol* 12: 33–45
- Levizzani V, Porcù F, Marzano FS, Mugnai A, Smith EA, Prodi F (1996) Investigating a SSM/I microwave algorithm to calibrate METEOSAT infrared instantaneous rain-rate estimates. *Meteorol Appl* 3: 5–17
- Lighthill MJ, Whitham CB (1995) On kinematic waves, 1, flood movement in long rivers. *P Roy Soc Lond Ser A* (229): 281–316
- Marshall J, Palmer W (1948) The distribution of raindrops with size. *J Meteorol* 5: 165–166
- Martz LW, Garbrecht J (1992) Numerical definition of drainage network and subcatchment areas from digital elevation models. *Comput Geosci* 18(6): 747–61
- Martz LW, Garbrecht J (1993) Automated extraction of drainage network and watershed data from digital elevation models. *Water Resour Bull* 29(6): 901–08
- Marzano FS, Turk J, Ciotti P, Di Michele S, Pierdicca N (2001) Potential of combined spaceborne microwave and infrared radiometry for near real-time rainfall attenuation monitoring along earth satellite. *Int J Satell Commun* 19(4): 385–412
- Marzano FS, Mugnai A, Turk J (2002a) Precipitation retrieval from spaceborne microwave radiometers and combined sensors. In: Marzano FS, Visconti G (eds) *Remote sensing of atmosphere and ocean from space*. Kluwer Academic Publ., Dordrecht, pp. 107–26
- Marzano FS, Fionda E, Ciotti P, Martellucci A (2002b) Ground-based multi-frequency microwave radiometry for rainfall remote sensing. *IEEE Trans Geosci Rem Sens* 40: 742–59
- Marzano FS, Palmacci M, Cimini D, Giuliani G, Turk JF (2004a) Multivariate statistical integration of satellite infrared and microwave radiometric measurements for rainfall retrieval at the geostationary scale. *IEEE Trans Geosci Remote Sens* 42(4): 1018–32

- Marzano FS, Picciotti E, Vulpiani G (2004b) Rain field and reflectivity vertical profile reconstruction from C-band radar volumetric data. *IEEE Trans Geosci Rem Sens* 42(4): 1033–46
- Marzano FS, Cimini D, Coppola E, Verdecchia M, Levizzani V, Tapiador F, Turk JF (2005) Satellite radiometric remote sensing of rainfall fields: multi-sensor retrieval techniques at geostationary scale. *Adv Geosci* 2: 267–72
- Memmo A, Faccani C, Ferretti R, Di Michele S, Frank Marzano (2006) Evaluation of radiative transfer schemes for mesoscale model data assimilation: a case study. *Adv Geosci* 7: 193–98
- Miller SW, Arkin PA, Joyce R (2001) A combined microwave infrared rain rate algorithm. *Int J Remote Sens* 22: 3285–307
- Montopoli M, Marzano FS, Vulpiani G, Fornasiero A, Alberoni PP, Ferraris L, Rebora N (2006) Spatial characterization of raincell horizontal profiles from C-band radar measurements at mid-latitude. *Adv Geosci* 7: 285–92
- Overtone DE (1964) Mathematical refinement of an infiltration equation for watershed engineering. ARS41-99, Dept. Agriculture, Agriculture Research Service, U.S.D.A.
- Packard NH, Wolfram S (1985) *J Stat Phys* 38: 901–46
- Pierdicca N, Pulvirenti L, Marzano FS, d'Auria G, Basili P, Ciotti P (2004) Intercomparison of inversion algorithms to retrieve rain-rate from SSM/I by using an extended validation set over the Mediterranean area. *IEEE Trans Geosci Rem Sens* 42(10): 2226–39
- Reisner J, Rasmussen R, Bruintjes R (1998) Explicit forecasting of supercooled liquid water in winter storms using the MM5 mesoscale model. *Q J R Meteorol Soc* 124: 1071–107
- Rivolta G, Marzano FS, Coppola E, Verdecchia M (2006) Artificial neural-network technique for precipitation nowcasting from satellite imagery. *Adv Geosci* 7: 97–103
- Roth G, Boni G, Giannoni F, Rudari R (2004) On the role of a hydrologic model in regional precipitation and flood frequency analyses. *EOS Trans AGU* 85(17): JA259
- Rotunno R, Ferretti R (2001) Mechanism of intense Alpine rainfall. *J Atmos Sci* 58: 1732–49
- Serafin S, Ferretti R (2007) Sensitivity of a mesoscale model to microphysical parameterizations in the MAP-SOP IOP2b and IOP8. *J Applied Met Clim* (in press)
- Siccardi F, Boni G, Ferraris L, Rudari R (2005) A hydro-meteorological approach for probabilistic flood forecast. *J Geophys Res* 110: D05101; DOI: 10.1029/2004JD005314
- Singh VP, Yu FX (1990) Derivation of infiltration equation using systems. Approach J Irrigation Drainage Eng 116(6): 837–58
- Singh VP, Frevert DK (2002) Mathematical models of small watershed hydrology and application. Water Resource Publications, LLC, Highlands Ranch, Colorado, USA
- Tapiador FJ, Kidd C, Levizzani V, Marzano FS (2004a) A neural networks-based PMW-IR fusion technique to derive half hourly rainfall estimates at 0.1° resolution. *J Appl Meteor* 43: 576–94
- Tapiador FJ, Kidd C, Hsu KL, Marzano FS (2004b) Neural networks in satellite rainfall estimation. *Meteorol Appl* 11: 1–9
- Thorntwaite CW, Mather JR (1957) Instructions and tables for computing potential evapotranspiration and the water balance. *Publications in Climatology*, Vol. 10. Laboratory of Climatology, Drexel Institute of Technology, 311 pp
- Todini E (1996) The Arno rainfall-runoff model. *J Hydrol* N 175: 339–82
- Todini E, Ciarrapica L (2002) The TOPKAPI model, mathematical model for large watershed hydrology. WRP Edition
- Tomassetti B, Coppola E, Verdecchia M, Visconti G (2005) Coupling a distributed grid based hydrological model and MM5 meteorological model for flooding alert mapping. *Adv Geosci* 2: 59–63
- Troen I, Mahrt L (1986) A simple model of the atmospheric boundary layer: sensitivity to surface evaporation. *Bound Lay Meteor* 37: 129–48
- Turcotte R, Fortin JP, Rousseau AN, Massicotte W, Villeneuve JP (2001) Determination of the drainage structure of a watershed using a digital elevation model and a digital river and lake network. *J Hydrol* 240: 225–42
- Turk JF, Rohaly G, Hawkins J, Smith EA, Marzano FS, Mugnai A, Levizzani V (2000) Meteorological applications of precipitation estimation from combined SSM/I, TRMM, and geostationary satellite data. In: Pampaloni P (ed) *Microwave radiometry and remote sensing of the environment*. VSP Int. Sci. Publisher, Utrecht, pp. 353–63
- Vicente GA, Scofield RA, Menzel WP (1998) The operational GOES infrared rainfall estimation technique. *Bull Amer Meteor Soc* 79: 1883–98
- Vulpiani G, Marzano FS, Chandrasekar V, Lim S (2005) Constrained iterative technique with embedded neural-network for dual-polarization radar correction of rain path attenuation. *IEEE Trans Geosci Remote* 43: 2305–14